Biosensors and Bioelectronics 184 (2021) 113235

Contents lists available at ScienceDirect

Biosensors and Bioelectronics

journal homepage: http://www.elsevier.com/locate/bios

Multi-stage responsive peptide nanosensor: Anchoring EMT and mitochondria with enhanced fluorescence and boosting tumor apoptosis

Yuwei Tian [a,1], Limin Zhang [a,1], Fangjie Liu [a], Minxuan Wang [a], Lingyun Li [a], Mingmei Guo [a], Hangyu Xu [a], Zhiying Yu [b], Weizhi Wang [a,*]

[a] Key Laboratory of Medical Molecule Science and Pharmaceutics Engineering, Ministry of Industry and Information Technology, School of Chemistry and Chemical Engineering, Beijing Institute of Technology, Beijing 100081, PR China
[b] National Center for Nanoscience and Technology, Beijing 100190, PR China

ARTICLE INFO

Keywords:
Multi-stage responsive
Peptide recognition
Receptor induced self-assembly
EMT sensor
Mitochondria

ABSTRACT

Epithelial-mesenchymal transition (EMT) is closely related to tumor metastasis and invasion. Thereinto, mesenchymal tumor mitochondria are the critical target for tumor inhibition. Therefore, real-time *in vivo* monitoring of EMT as well as inhibiting mesenchymal tumor mitochondria is of great diagnosis and therapy significance. Herein, we construct a multi-stage recognition and morphological transformable self-assembly-peptide nano biosensor ^{N}DRP which can response the EMT marker and specifically damage the mesenchymal tumor cell *in vivo*. This nano-molar-affinity sensor is designed and screened with sensitive peptides containing a molecular switching which could be specifically triggered by the receptor to achieve the vesicle-to-fibril transformation in living system with enhanced fluorescent signal. ^{N}DRP nanosensor could target the tumor lesion in circulatory system, recognize mesenchymal tumor marker DDR2 (Discoidin domain receptor 2) in cellular level and specifically achieve mitochondria in subcellular level as well as damaged mitochondria which could be applied as a *in vivo* theranostic platform.

1. Introduction

Smart-nanostructure-derived nanosensors for biomedical applications such as tumor detection, microenvironment response and controlled release have been developed for years (Li et al., 2019b; Liu et al., 2015; Song et al., 2014). Among them, *in vivo* nanosensing system can accurately reflect the real-time physiological and pathological conditions in living system (Park et al., 2020; Peri et al., 2021; Zhang et al., 2018b). However, it is difficult for a smart-nanostructure to keep their delicate structure in complicated real biosystem, which limited their clinical translation (Ying et al., 2019). One promising strategy is *in situ* construction of bioinspired nanostructures with sensitive response and enhanced signals. This presented an *in vivo* nanosensor some requests. Concretely, 1) it should accurately recognize lesion in the circulatory system; 2) it should specifically indicate the disease marker in cellular level and provide enhanced signals; 3) it should effectively interact with the pharmaceutical targets in subcellular level and realized therapy. Stimuli-responsive peptide self-assemblies (pSAs) are appropriate bioinspired nanostructures which can meet the above criterions. It is reported that pSAs-based nanosensors have the advantages of multi-covalent recognition and biocompatibility, which enabled the sensitive detection at the single-molecular level in living systems (Li et al., 2019a). Furthermore, tumor-environment-responsive and morphology-transformable pSAs could indicate the tumor progression (Liu et al., 2020; Zhang et al., 2018a). All these achievements boost the *in vivo* performance of pSAs-based nanosensors in tumor diagnosis and therapy (Lim et al., 2018). Most of them are designed based on building blocks. The self-assembly unit and the response unit are mainly from some natural original proteins such as the KLVFF sequence from the Alzheimer disease related proteins (Luo et al., 2020; Pigliacelli et al., 2019; Shuaib et al., 2020). Furthermore, these units are relatively independent among each other and difficult to play synergistic sensitivity for all the segment units. Besides recognition, another important element is sensitive signal. Fluorescence boosting sensing shows excellence in simplicity and sensitivity, which effectively enhance the detection of nanosensor in complicated system. Recent years, many

* Corresponding author.
E-mail address: wangwz@bit.edu.cn (W. Wang).
[1] These authors contributed equally.

https://doi.org/10.1016/j.bios.2021.113235
Received 24 January 2021; Received in revised form 30 March 2021; Accepted 6 April 2021
Available online 19 April 2021

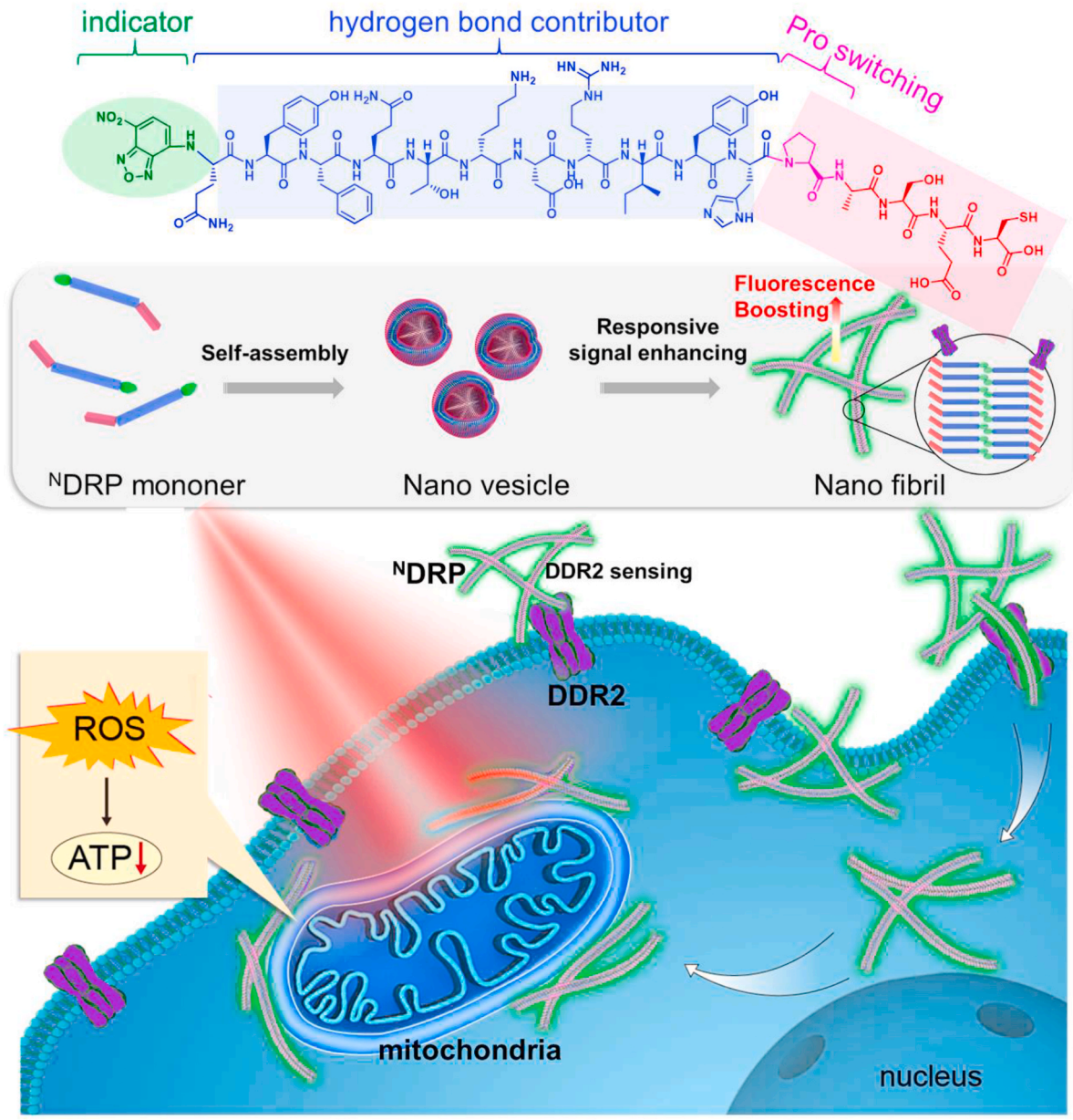

Fig. 1. Schematic illustration for the nanosensor. ^{N}DRP could first recognize and trigger by DDR2, then transform from nano vesicle into nano fibril and emit enhanced fluorescent signal. ^{N}DRP could also achieve and damage mitochondria.

pSAs-fluorophore conjugated platforms for *in vivo* recognition and detection are made great progress (Yang et al., 2016; Yue et al., 2016). Hence, we envision that developing an *in vivo* peptide-fluorescence nanosensor system of which all the elements are integrated through rational design and high-throughput screening (Hartgerink et al., 2001; Zhang, 2003). One sequence could successively recognize the lesion, detect the state of cell and monitor the organelle by the multi-stage recognition and microenvironment-induced morphology formation (MIMF). The effective and synergistic system would improve the detection and sensing performance (James et al., 2019; Shin et al., 2018).

Epithelial-mesenchymal transition (EMT) is closely related to tumor invasion and metastasis (Brabletz et al., 2018; Tsai et al., 2012). The monitoring of the EMT-associated tumor markers could be used as highly specific indicators of malignancy. Discoidin domain receptor 2 (DDR2) is a 130 kDa transmembrane protein, which is considered as a promising cell-membrane target for mesenchymal cancer (Ren et al., 2014; Tu et al., 2019; Zhang et al., 2013). Furthermore, it is more attractive to inhibit EMT on the basis of detection. Mitochondria are the energy and reactive oxygen species (ROS) center of the cells (Jeena et al., 2019; Shah et al., 2014). Studies have found that through regulating the ROS or membrane potential of mitochondria could activate the endogenous pathways for tumor apoptosis (Jajoo et al., 2016; Wei et al., 2018; Zhang et al., 2020). It is reported the fibrous nanostructures have larger hydrophobic area, stronger cell permeability and excellent entangled ability, which could significantly enhance the fluorescence intensity in living system (Cheng et al., 2019). In this case, nanovesicle-to-nanofibril transformation may boost the fluorescent signal and increase the sensitivity of sensing system. Therefore, it is desirable to develop a multi-stage responsive pSAs-fluorophore nanosensor which recognize EMT, response the DDR2 marker and monitor the mitochondria in both successively and specific way would achieve intelligent *in vivo* sensing.

In this study, we design and screen a smart pSAs-fluorophore platform ^{N}DRP which could target EMT marker DDR2 and mitochondria consecutively to achieve biosensing in living system. ^{N}DRP is screened

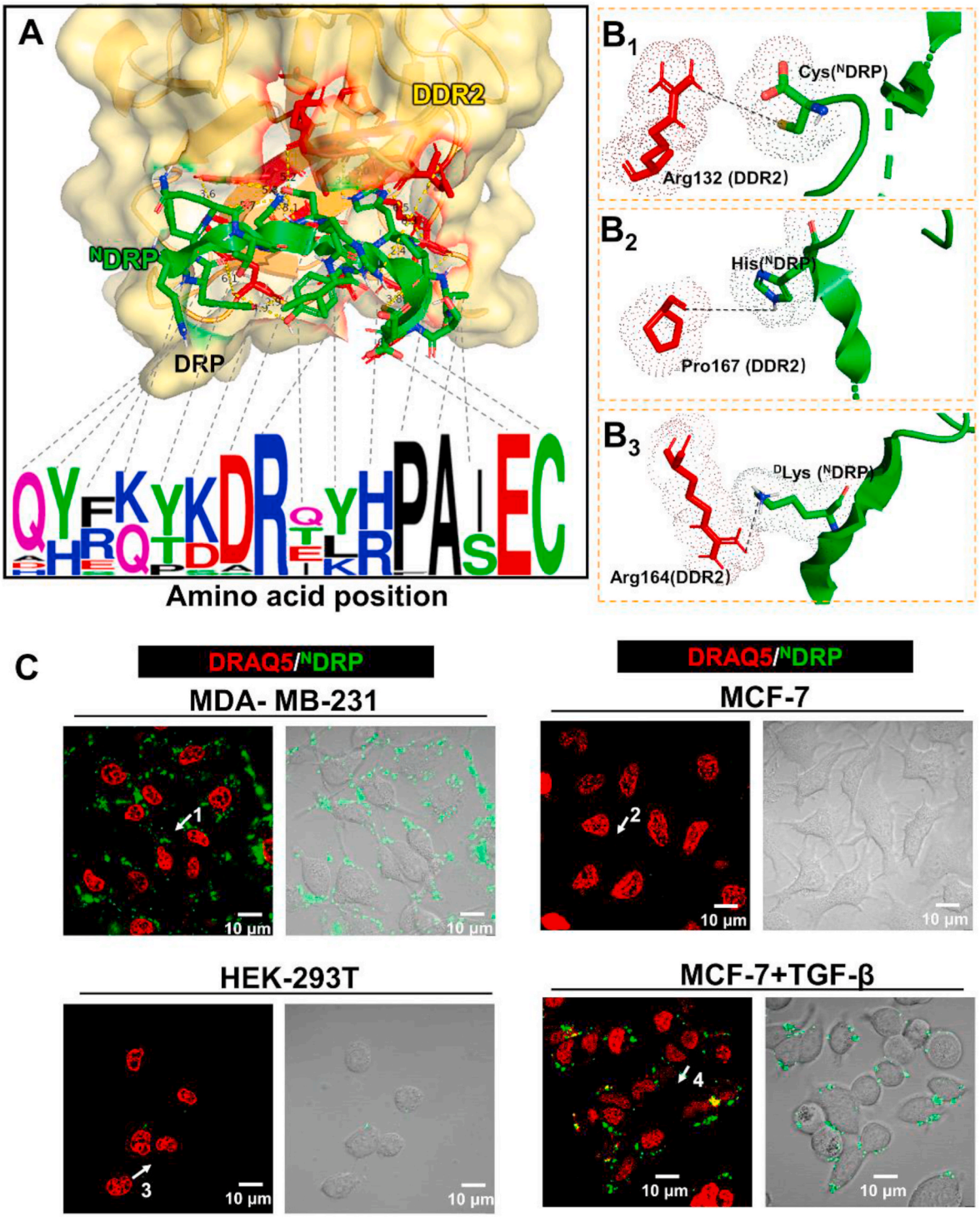

Fig. 2. The screening and binding of ^{N}DRP. (A) ^{N}DRP/DDR2 complex predicted with crystal molecular docking. (B) The main hydrogen bonds between ^{N}DRP and DDR2. (C) Confocal images of ^{N}DRP treated cells.

out from a high-throughput peptide library with a brand-new peptide sequence DRP and a hydrophobic responsive fluorophore 4-chloro-7-nitro-2,1,3-benzoxadiazole (NBD). DRP peptide have a Pro-based 'switching' which could be induced by receptor in the living system. NBD emitting stronger fluorescence in the hydrophobic environment which could be employed as an assembly-responding signal. In the presence of DDR2, the morphology ^{N}DRP could be triggered from nanovesicles to nanofibrils, along with an enhanced volume of the hydrophobic cavity, which boost the fluorescent signal of NBD. Furthermore, the reassembled nanofibrils could penetrate into the cells and targeting the mitochondria and damage the mesenchymal mitochondria in a specific manner. The multistage peptide-based nanosensor could be used for the detection of EMT-associated progression and perform the tumor theranostics (Fig. 1).

2. Materials and methods

2.1. Materials and reagents

9-Fluorenylmethoxycarbonyl (Fmoc)-protected amino acid, Wang resin and 2-(3′-N-oxo-benzotriazole)-1,1′,3,3′tetramethylurea hexafluoro phosphate (HBTU) were purchased from GL Biochem. Tentagel resin was purchased from Rapp Polymere. Triisopropylsilane (Tips) was from Sigma-Aldrich. Cyanogen bromide (BrCN) was from J&K Chemicals. Trifluoroacetic acid (TFA), thiazolyl blue tetrazolium bromide (MTT), Chlorin e6 (Ce6) and cell lysate were purchased from Sigma-Aldrich. Tween-20 was purchased from Merck. 4-Chloro-7-nitrobenzo-2-oxa-1,3-diazole (NBD-Cl) was purchased by MedChemExpress. Hoechst 33342, DRAQ5™, 1-(3-Dimethylaminopropyl)-3-ethylcarbodiimide hydro chloride (EDC), N-Hydroxysuccinimide (NHS), piperidine, dimethylformamide (DMF) were purchased from Sigma-Aldrich. Biotin Labeling Kit was from Dojindo Molecular Technologies. TGF-β was from T&L Biological Technology. Acetonitrile, methanol and were purchased from Thermo Fisher. 2′,7′-Dichloro-dihydrofluorescein diacetate (DCF-DA) and antibodies against β-actin were purchased from Sigma-Aldrich. BCA Protein Assay Kit and dimethyl sulfoxide (DMSO) were from Solarbio. ATP Bioluminescence Assay Kit was purchased from Beyotime Biotechnology. Streptavidin coated magnetic beads were purchased from Tianjin BaseLine ChromTech Research Center. Western Blot Detection Kit was purchased from Thermo Fisher. N,N-Diisopropylethylamine (DIEA) was from Aladdin. MitoTracker Green was from Cell Signaling Technology. LysomeTracker, Endoplasmic Reticulum Tracker (ERTracker) were from Solarbio. Annexin V-FITC Apoptosis Detection Kit was purchased from Invitrogen. DDR2 protein and DDR2 antibody were purchased from Sino Biological. The human breast cancer cell line MDA-MB-231 and MCF-7, the human kidney epithelial cell line HEK-293T were purchased from Cell Center of Chinese Academy of Medical Sciences. Female BALB/c nude mice were purchased from Vital River Laboratory Animal Technology Co., Ltd. All reagents were used as received, and solvents were purified according to general procedures before use.

2.2. The process of TGF-β induced DDR2 up regulation

MCF-7 cells were seeded into culture dish for 24 h. Then the cells were digested with trypsin and centrifuged for 3 min. When the digestion step was completed, the cells were transferred into the Opti-MEM medium. The transfection operation was performed on electroporator (NEPA21 Super Electroporator). Added the electro-mixed liquid to the electro-rotor cup and put it into the electro-rotor cup cavity. Then the electric transfer procedure was executed. After the electroporation step, the MCF-7 cells were transferred to culture dish and cultured for 48 h.

2.3. Living tumor cells imaging using ^{N}DRP

^{N}DRP (0.5 mM) was dissolved in DMEM medium. MDA-MB-231 cells, MCF-7 cells and HEK-293T cells were individually incubated with DRAQ5™ (100 μL) in dark at 4 °C for 25 min. Then ^{N}DRP solution (100 μL, 1 mg/mL) was added to the cells and incubated in the dark at 4 °C for 10 min. Finally, the cells were washed three times with cold PBS. Confocal fluorescence imaging was performed on confocal laser scanning microscope (ZEISS LSM710). The objective lens used for imaging was 63× oil-immersion objective.

2.4. Subcellular localization of ^{N}DRP

MDA-MB-231 cells and MCF-7 cells were individually seeded in confocal dish with DMEM (100 μL) at 37 °C for 24 h. Added the ^{N}DRP (20 μM) to DMEM (1 mL). Then added the ^{N}DRP solution to the dish and cultured for 2 h. The MitoTracker (1 μM) was dissolved in DMEM (500 μL). Then added the MitoTracker solution (200 μL) to the confocal dish and incubated for 20 min. Next, the cells were washed three times with PBS, finally performed on ZEISS LSM710 confocal laser scanning microscope.

2.5. Detection of intracellular ATP release level

The MDA-MB-231 cells were seeded into cell culture dish for 24 h. The ^{N}DRP (20 μM) was dispersed in DMEM (1 mL). Then the ^{N}DRP solution (200 μL) was added to the culture dish for 6 h. The ^{N}DRP-treated group was exposed to the light for 20 min (460 nm, 20 mW/cm^2). The ^{N}DRP treating group without light irradiation and normal saline-treated group were served as controls. Finally, the cells were treated with lysis buffer for 10 min and the ATP content of each group was measured.

3. Results and discussion

3.1. Design, synthesis and the screening of the high-content peptide library

We constructed the peptide library with a capacity of 10^6 using the "one-bead-one-compound" combinatorial chemistry approach. The detailed library design is listed in Fig. S1. Generally, the sequence is alternated with β-sheet-forming residues (Y, I, F, T et al.) and hydrophilic ones (R, D, K et al.). Such structures are beneficial for self-assembly. Besides, hydrophilic residues may facilitate the affinity recognition in living systems. In especial, we set a 'molecular switching' Proline residue in the sequence induce as a trigger point of the nano sensor (Pro switching in Fig. 1). The side chain atoms N (Pro) has almost no contribution to the formation of hydrogen bonds and the rings of Pro cannot match the stable assembly frameworks. We speculate that the Pro switching would be affected by external force which may induce the self-assembly morphology transformation. 4-Nitro-2,1,3-Benzodiazole (NBD), a hydrophobic cavity indicator, was introduced in the screening process to indicate the self-assembly (Jeena et al., 2017). Combined with the magnetic/fluorescent-assisted sorting and *in situ* microfluidic screening based on our previous works, the DDR2-targeting peptide with self-assembly ability was emerged from the sequence map alignment (Figs. S2–S4) (Wang and Hu, 2019; Wang et al., 2014). The peptide is denoted as ^{N}DRP (sequence: NBD-QYFQT^{D}KD^{D}RIYHPASEC, Fig. 1). ^{N}DRP was *de novo* synthesized and purified (Figs. S5 and S6).

3.2. Affinity and specificity characterization of ^{N}DRP

The affinity and specificity of ^{N}DRP targeted DDR2 are evaluate in molecular level and cellular level. As shown in molecular docking (Fig. 2A), the intermolecular forces between ^{N}DRP and DDR2 are dominated by hydrogen bonds. In particular, the hydrogen bonds are mainly contributed by the interaction between Arg132 (DDR2)-Cys (^{N}DRP) (Fig. 2B$_1$), Pro167 (DDR2)-His (^{N}DRP) (Fig. 2B$_2$) and Arg164 (DDR2)-^{D}Lys (^{N}DRP) (Fig. 2B$_3$). The dissociation constant (K_D) value of DRP was determined by surface plasmon resonance imaging (SPRi, Fig. S7) and was calculated as 30.8 nmol/L, indicating a satisfactory affinity toward DDR2. We further investigated the specificity of ^{N}DRP at the cellular level by confocal laser scanning microscopy (CLSM). The mesenchymal-derived human breast cancer cell line MDA-MB-231 (DDR2 overexpression) was chosen as the positive cell model (Western blot bands of all cells are shown in Fig. S8). The epithelial-derived human breast cancer cell line MCF-7 (DDR2 low-expression) and normal cell line HEK-293T were served as controls. Cells were individually incubated with ^{N}DRP (ex/em = 488/525 nm). DRAQ5™ (ex/em = 646/697 nm) is employed as a nuclei indicator. As shown in Fig. 2C, MDA-MB-231 cells have a distinct signal on membranes while MCF-7 cells and HEK-293T cells show almost no signal. Furthermore, we used cell induction strategy to mimic the EMT process. TGF-β (transforming growth factor β) was added to MCF-7 cells which facilitated the mesenchymal transition (DDR2 up-regulation) (Walsh et al., 2011). A significant brighter fluorescent signal was still observed. For

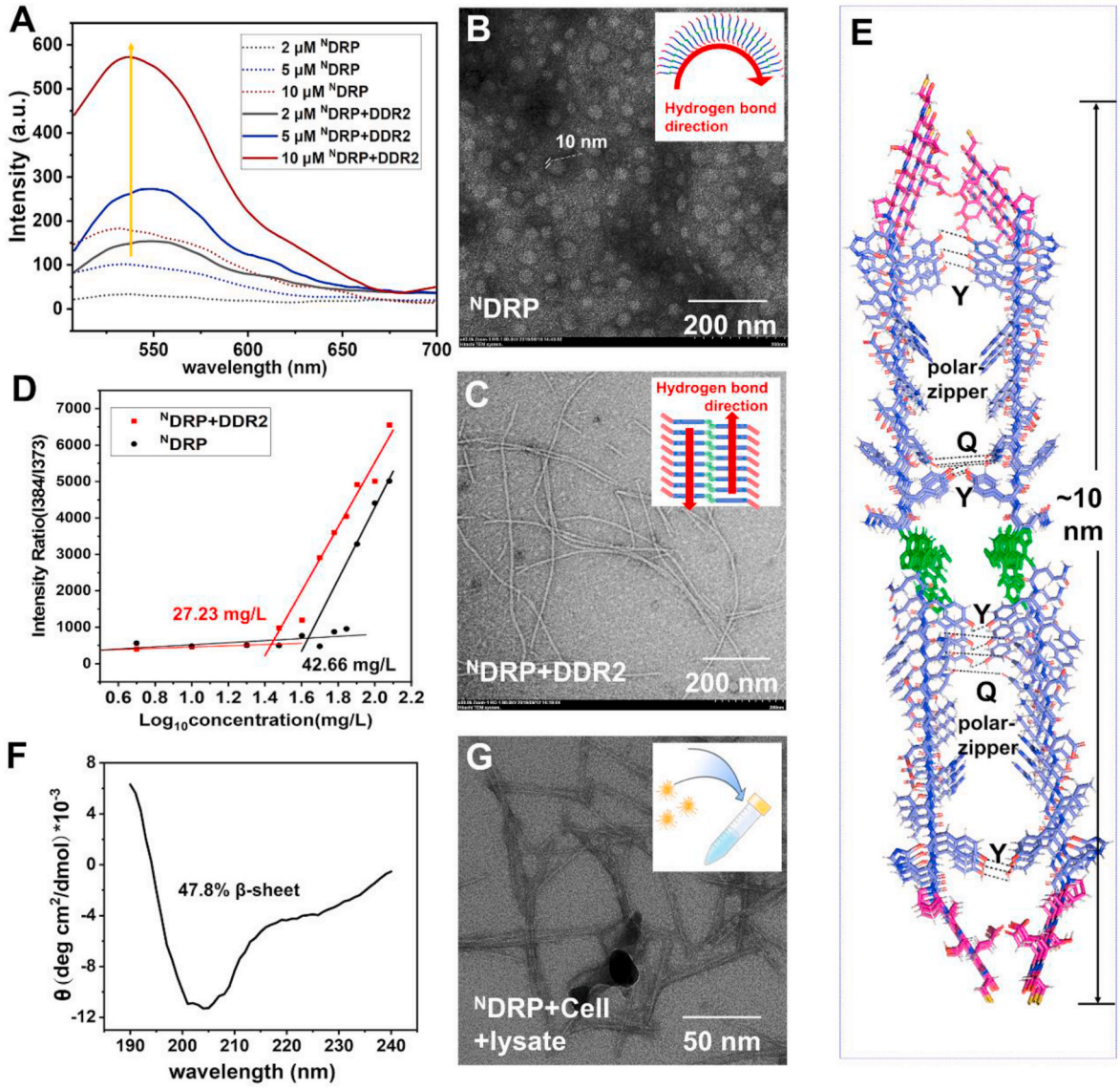

Fig. 3. Nanofibrillar transformation and fluorescence boosting of ^{N}DRP. (A) Fluorescence emission of ^{N}DRP at various concentration with or without DDR2 co-incubation. (B) The TEM image of ^{N}DRP. (C) The TEM image of ^{N}DRP with DDR2 co-incubation. (D) The CAC shifting of ^{N}DRP with and without the presence of DDR2. (E) The formation of polar zippers between the neighboring β-sheets. (F) The circular dichroism (CD) of ^{N}DRP cultured with DDR2 protein. (G) The TEM micrograph for ^{N}DRP in the MDA-MB-231 cell lysate.

quantitative comparison, fluorescence intensity profiles along through the white arrows were also illustrated (Fig. S9). To further evaluate the accurate binding site, a blocking assay was carried out. It is shown that pre-incubation with DDR2-antibody, the binding efficiency of ^{N}DRP on MDA-MB-231 cells was obviously decreased comparing with the un-treated ones (Fig. S10). These observations clearly indicated that ^{N}DRP can specifically bind to DDR2 with a high affinity which may developed into an EMT sensor in living system.

3.3. Receptor-triggered morphology transformation, fluorescence boosting and according mechanism explanation

Since ^{N}DRP owns affinity and specificity. We evaluate the DDR2-induced self-assembly behavior and the fluorescence boosting ability. For the ^{N}DRP only, when ^{N}DRP formed a well-organized hydrophobic cavity, the fluorescence of NBD would be lighted. The curves in Fig. 3A indicated that the fluorescence intensity of ^{N}DRP is proportional to the concentration of solutions. ^{N}DRP exhibited a nanovesicle structure with an average diameter of ~50 nm (Fig. 3B, dynamic light scattering in Fig. S11). When co-incubated with DDR2, ^{N}DRP nanovesicles are transformed into nanofibrils (Fig. 3C). In the presence of DDR2, the fluorescence signal of NBD has effectively enhanced (Fig. 3A) in the same concentration. This may be caused by the nanofibril-formation and increasing of the hydrophobic area. The critical assembly concentration (CAC) could also prove this. As shown in Fig. 3D, the CAC of the ^{N}DRP itself is 42.66 mg/L while that decreased into 27.23 mg/L when DDR2 induced. Self-assembly preferred to occur when DDR2 induced. ^{N}DRP owns the receptor-triggered morphology-transformation ability, which displays notable advantages in enhancement of the fluorescence signal. We further explain the assembly-transformation mechanism. In ^{N}DRP, segment QYFQT^{D}KD^{D}RIYH is consisting of alternate hydrophilic and hydrophobic residues, which is easily to form β-sheet structure through hydrogen bonds between the adjacent strands (Fig. S12). The side chains of residues such as Y and Q will form 'polar-zipper' between adjacent β-sheets through intermolecular hydrogen bonds, which facilitate the lateral growth of the vesicles (Fig. 3E) (Wang et al., 2018; Zhao et al., 2020). The shell thickness of the vesicles was observed as ~10 nm (transmission electron microscopy (TEM) photograph in Fig. 3B),

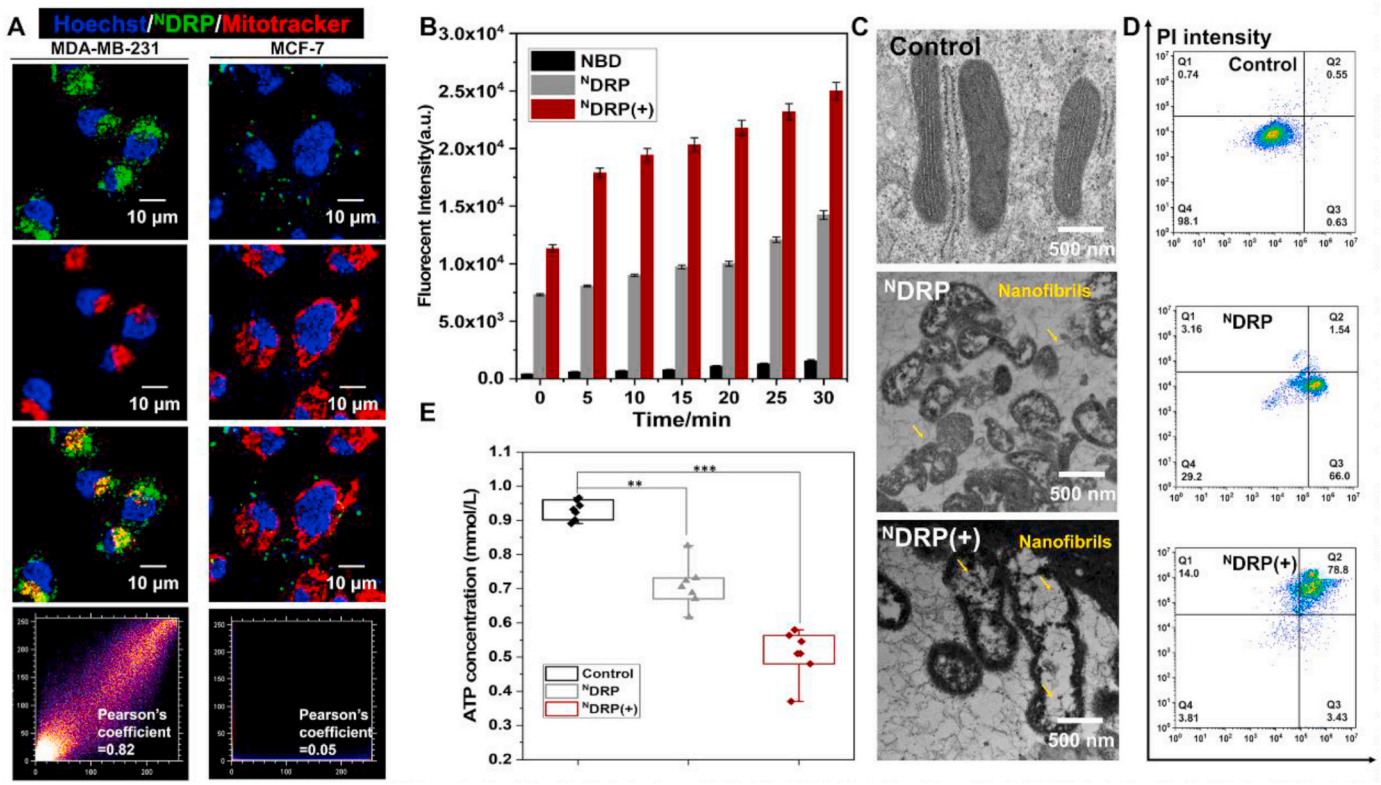

Fig. 4. Detection of mitochondria targeting behavior and the mesenchymal-tumor-cell killing effect of ^{N}DRP. (A) Mitochondrial localization analysis of MDA-MB-231 cells and MCF-7 cells individually treated with ^{N}DRP (20 μM). (B) Fluorescence intensity of DCF when MDA-MB-231 cells were individually incubated with NBD, ^{N}DRP and ^{N}DRP with 20-min light irradiation. (C) TEM images of mitochondria isolated from MDA-MB-231 cells as well as being incubated with ^{N}DRP and ^{N}DRP(+), respectively. (D) Flow cytometric analysis of ^{N}DRP was obtained with Annexin/PI staining on MDA-MB-231 cells after treating with ^{N}DRP(+). (460 nm, 20 mW/cm^2, 20 min). (E) ATP secreting level in MDA-MB-231 cells without and with light irradiation. Control experiment was performed with PBS. (data were presented as mean ± SD (n = 7); **P < 0.05, ***P < 0.01).

indicating that the vesicle form a bilayer and interdigital structure in a 'tail-to-tail' manner through hydrogen bonds and hydrophobic interaction. As the design of the trigger point, Pro is incompatible with hydrogen bond and the following ASEC segment could not continue the formation of β-sheet along the peptide strands. Therefore, the segments exist in the form of random coil. (47.8% β-sheet shown in circular dichroism (CD) in Fig. 3F). Hence, this vesicle is less stable and has the chance to be induced by external influence. When ^{N}DRP recognized DDR2, the strong affinity between them will destroy the mechanical balance of the original assemblies, and the vesicles would disassemble. The monomers or oligomers will bound to DDR2 as 'seeds' to initiate the re-assembly. Their degree of freedom is decreased and would eliminate the original curvature required for vesicle formation. Therefore, it would finally twist into nanofibrils under the action of static electricity and chirality (Fig. 3C). These nanofibrils display cross β-sheet structure, in which the β-strands are arranged perpendicular to the fibril alignment axis (Dobson, 2003). Furthermore, we observe *in situ* self-assembly in the living system. When incubated with ^{N}DRP, MDA-MB-231 cells were lysed and characterized by TEM. We can clearly find the existence of nanofibrils (Fig. 3G). The cell lysate was characterized by the mass spectra and we find the double-charged, triple-charged and tetra-charged m/z (mass-to-charge ratio) peaks of ^{N}DRP in the lysate. (Fig. S13). All these results persuasively proved that ^{N}DRP can target DDR2 as well as be induced and transformed in a specific manner.

3.4. Mitochondrial targeting and damage by ^{N}DRP on mesenchymal original tumor cells

In order to construct an integrated platform combined with diagnosis and therapy. We further develop ^{N}DRP into a mitochondrial targeting reagent. First, we examine the organelle-location of ^{N}DRP. As the CLSM images shown in Fig. 4A and Fig. S14, in MDA-MB-231 cells, ^{N}DRP can overlap well with the MitoTracker (mitochondria indicator, ex: 490 nm; em: 516 nm), showing much higher Pearson's coefficient (0.82) than those of MCF-7 cells (Pearson's coefficient = 0.05). However, the co-localization rate of ^{N}DRP with other organelles are much lower (Fig. S15). We explain the mitochondria-targeting ability by DDR2 mediation and charge interaction. In the nano fibril structures, one of the hydrophilic head with the sequence 'QT^{D}KD^{D}R' exposed. This segment has the isoelectric point of 10.91 and shows positive charge, which is likely to bind the negatively-charged inside membrane of mitochondria (Fan et al., 2019; Song et al., 2017). Additionally, the lipophilicity of the ^{N}DRP provide another reason to bind mitochondria. We further evaluate whether it can damage mitochondria even kill tumor cells. It is recognized that mitochondria-targeted nano systems can interfere with ROS homeostasis and further induce apoptosis. Some reports showed that NBD could be irradiated and generated ROS which may be boosting the photodynamic therapy (PDT) (Otake et al., 2018). We evaluate the ability of ^{N}DRP to generate ROS under 460 nm-irradiation *in vitro* (^{N}DRP(+)) in MDA-MB-231 cells. ^{N}DRP without irradiation and NBD were served as controls. 2′, 7′-Dichloro-dihydrofluorescein diacetate (DCF-DA) assay was employed to detect ROS level in cellular level. As shown in Fig. 4B, the fluorescent intensity of the ^{N}DRP-treated group increased dramatically, indicating the generation of ROS specifically in mesenchymal tumor cells. Also, the TEM images (Fig. 4C) showed that the morphology of mitochondria in MDA-MB-231 cells became swollen after incubation with ^{N}DRP. Moreover, the ^{N}DRP(+) illustrated more serious mitochondria damage. ^{N}DRP nanofibrils are clearly visible inside the mitochondria. It is indicated that ^{N}DRP nanofibrils kept stable through the cell penetration and

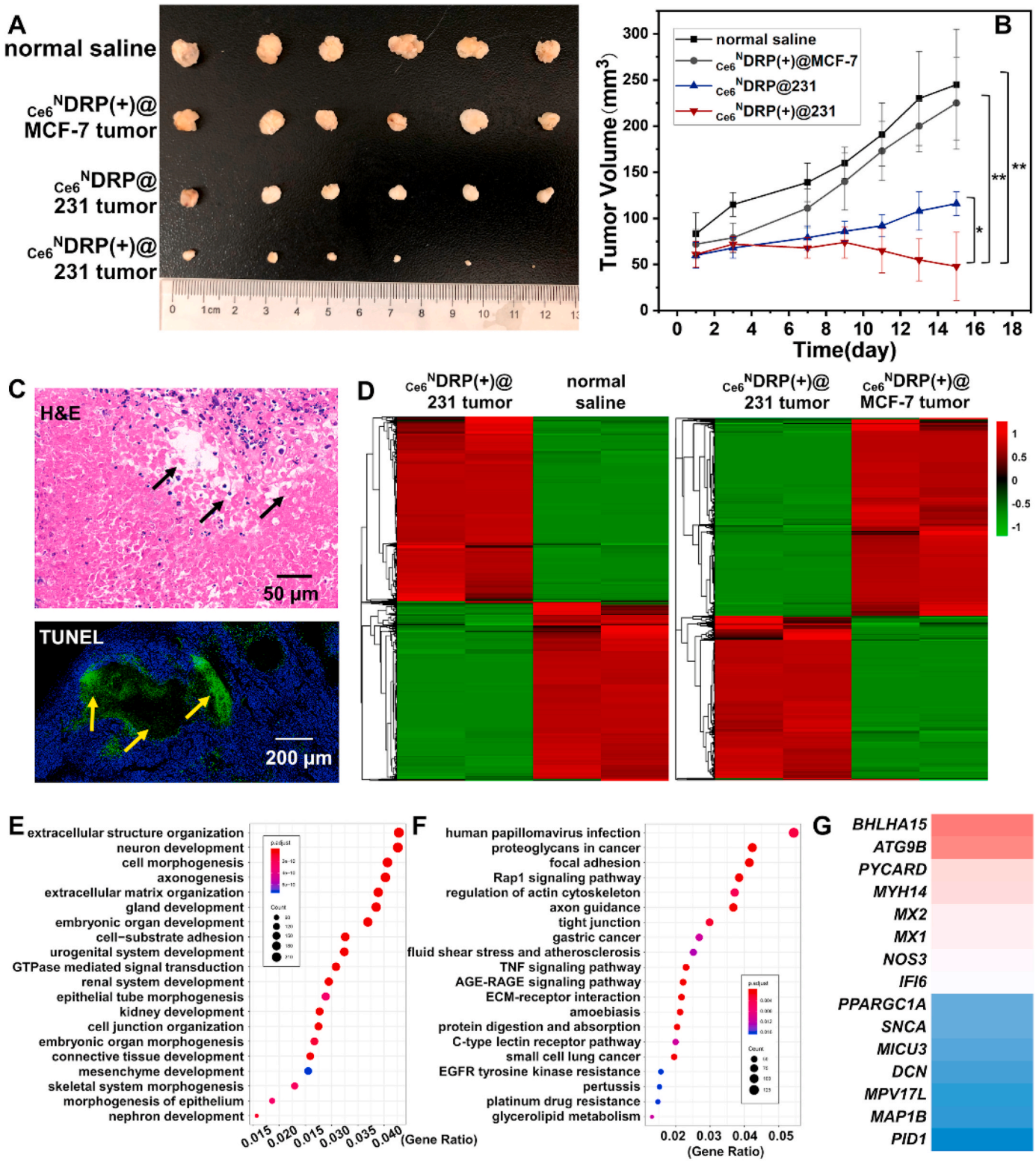

Fig. 5. Tumor treatment efficacy of ^{N}DRP. (A) Photograph of excised tumors at the therapy terminal. (231 is the abbreviation for MDA-MB-231.) (B) Tumor volume changing curves during the cure process. Treated groups displayed the statistically significant differences from the control group, as measured by the Student's t-test (*$p < 0.1$, **$p < 0.05$). (C) Analysis of the tumor slices with H&E and TUNEL staining in therapeutic condition (^{N}DRP(+)). (D) Differential gene expression heatmaps of tumors in different treating groups. (E) BP map for GO analysis of altered genes in $^{N}_{Ce6}$DRP(+)-treated group. (F) KEGG analysis of altered genes in $^{N}_{Ce6}$DRP (+)-treated group. (G) The significant mitochondrial-related genes.

mitochondria internalization process. Furthermore, it is indicated that over-generated ROS affect the mitochondrial membrane permeability, which caused the pressure changed inside and outside the mitochondria, so as to damage mitochondria. It is suggested that the ridges of mitochondria are disappeared and the mitochondria dysfunction caused by fibril conformation is responsible for cellular death. In addition, we evaluated the tumor-cell killing effect of ^{N}DRP *in vitro* by PI (Propidium Iodide) staining assay to quantitatively analyze the apoptosis. Notably in the flow cytometry in Fig. 4D, ^{N}DRP treatment induced 66% cells into early apoptosis and ^{N}DRP(+) treatment induced more than 78% mesenchymal tumor cell death. It is indicated that the mitochondria-targeting approach could kill tumor cells could be used for PDT. Since mitochondria are cells' powerpacks, we further tested the adenosine triphosphate (ATP) secreting level in cells. As shown in Fig. 4E, the content of ATP secreting by damaged mitochondria was significantly decreased. As expected, we could observe that the contribution of ^{N}DRP during the PDT process. These data strongly demonstrate that nanofibrillar structure on the surface of DDR2^{+} tumor cells are the significant factor to cell death. The cytotoxicity was measured by MTT assay. MDA-MB-231 cells were individually incubated with ^{N}DRP, DRP and NBD by the same concentration gradient solutions with or without light irradiation. Fig. S16 illustrated that ^{N}DRP(+) has a damage effect towards mesenchymal tumor cells in an apoptosis dependent way while all these control ones (including DRP(+), NBD(+), ^{N}DRP incubated with MCF-7 cells and HEK-293T cells) have little effects. It is further proved that all the components in ^{N}DRP play synergistic effect which could not only target mitochondria precisely but own the capacity for PDT.

3.5. Monitoring and RNA-seq analysis of the antitumor effect

To further explore the *in vivo* cancer treatment of ^{N}DRP, MDA-MB-231 xenograft tumor-bearing mice were served as positive model and randomly divided them into four groups (n = 6). In order to further enhance the *in vivo* PDT, we introduce a photosensitizer with an excitation wavelength in the near-infrared window. Ce6 was encapsulated into ^{N}DRP nano-system ($^{N}_{Ce6}$DRP). Mice were intravenously treated with $^{N}_{Ce6}$DRP(+) (under 808-nm laser irradiation), $^{N}_{Ce6}$DRP, and normal saline, respectively. MCF-7 xenograft tumor model treated by $^{N}_{Ce6}$DRP(+) was also severed as control. As shown in Fig. 5A and B, compared with the other groups, the tumor growth of the $^{N}_{Ce6}$DRP(+)-treated group was significantly inhibited when compared with that of the normal-saline-treated group. $^{N}_{Ce6}$DRP-treated group without irradiation display certain tumor inhibitory effects, indicating the significance of mitochondria targeting and damage ability. However, MCF-7 xenograft tumors were inhibited only a little under the same PDT treatment. These results indicated that the ^{N}DRP could evidently target as well as damage the mesenchymal tumor in a specific way. Meanwhile, the body weight of the mice in the $^{N}_{Ce6}$DRP(+)-treated group did not change significantly (Fig. S17), implying low toxicity. Additionally, the histological examination of the tumors was evaluated. As shown in Fig. 5C, hematoxylin-eosin (H&E) staining of the tumor demonstrated $^{N}_{Ce6}$DRP(+)-treated group showing obvious damage to tumor tissues, while other main organs showed no apparent morphological difference. In addition, the apoptosis of tumor cells was also detected by TUNEL assay. The tumor cell apoptosis of $^{N}_{Ce6}$DRP(+)-treated group was more obvious than other tissue slices (Fig. S18). Furthermore, pharmacokinetics and blood hemogram study were carried out after the $^{N}_{Ce6}$DRP injection. *In vivo* pharmacokinetics study was performed by monitoring the NBD signal (Zhang et al., 2016). As shown in Fig. S19, half-time of $^{N}_{Ce6}$DRP in blood circulation was ~3.12 ± 0.13 h. The *in vivo* retention could be ascribed to *in situ* receptor-mediated conformation. Blood chemistry detection and routine blood examination were also obtained (Fig. S20 and S21). There were no obvious difference compared with the normal blood samples. All these results suggested that the $^{N}_{Ce6}$DRP achieves high efficiency in PDT and has little side effects, thus showing a satisfactory theranostic efficacy.

We further evaluate the therapy effect of ^{N}DRP in transcriptome level. We used RNA-sequencing (RNA-seq) technique to draw genetic profiles in each treated group. $^{N}_{Ce6}$DRP(+)-treated MDA-MB-231 tumors were analyzed. Normal saline-treated groups and $^{N}_{Ce6}$DRP(+)-treated MCF-7 tumors were served as control. As shown in Fig. 5D, the heatmap of many altered genes were emerged from the differently treated groups. To confirm the number of differential genes among all the groups, the volcano plots in which the upregulated or downregulated genes marked with red and blue color by log2 fold-change were drawn (Fig. S22). In addition, Gene Ontology (GO) analysis and Kyoto Encyclopedia of Genes and Genomes (KEGG) were introduced to determine the molecular pathways affected by ^{N}DRP. As shown in Fig. 5E (Biological process, BP in GO analysis) and 5F (KEGG), we can clearly observe that the altered pathways are related with extracellular structure organization, TNF (tumor necrosis factor) signaling and extracellular matrix receptor interaction. These are initial signals for tumor metastasis, indicating that ^{N}DRP have affected the metastasis pathway through EMT recognition. We further analyze the cellular component and molecular function. As shown in Figs. S23 and S24, we find that the extracellular and intracellular related genes are both altered in $^{N}_{Ce6}$DRP(+) treated MDA-MB-231 tumor group. Compared with the $^{N}_{Ce6}$DRP(+)-treated mesenchymal group and epithelial group, the altered genes are related with cell adhesion binding, cell-cell junction and extracellular matrix collagen which are all contributed to the EMT (Figs. S25–S27). In especial, we observed key gene alternations related with mitochondria. We can clearly find upregulated autophagy-related genes in Fig. 5G, which play critical roles in the mechanism of positive regulation in mitochondrial autophagy. Moreover, these genes are mainly classified in tumor apoptosis and metabolism pathways, indicating the therapeutic effect of $^{N}_{Ce6}$DRP(+).

4. Conclusion

In conclusion, we designed a self-assembled peptide platform which could be induced into vesicle-to-fibril transformation which boost the detection signal as well as the curative effect. In this case, a simple and sensitive fluorescent sensor was developed for specifically recognize the epithelial-mesenchymal transition (EMT) and precisely bind to mitochondria and further induce apoptosis. This multi-stage responsive nanosensor system is prospectively developed into an integrated platform reagent for diagnosis and treatment in future.

Author contribution

The authors are declaring that all the following contribution descriptions are accurate and agreed by all authors.

Yuwei Tian: Methodology, Data Gathering;

Limin Zhang: Methodology and original draft preparation;

Fangjie Liu: Cellular imaging data gathering and revised manuscript editing;

Minxuan Wang: Animal data gathering;

Lingyun Li: Animal data gathering;

Mingmei Guo: Animal data gathering;

Hangyu Xu: Cellular imaging data gathering;

Zhiying Yu: Cellular imaging data gathering;

Weizhi Wang: Supervision, Conceptualization, Writing, Reviewing and Editing.

Declaration of competing interest

The authors declare that they have no known competing financial interests or personal relationships that could have appeared to influence the work reported in this paper.

Acknowledgments

The authors are grateful for financial support from National Key R&D Program of China (2018YFE0205400), National Natural Science Foundation of China (22074006, 21775031), Beijing Institute of Technology Research Fund Program for Young Scholars and Youth Innovation Promotion Association CAS (2019040). We thank Supercomputing Center of Chinese Academy of Science for their help on molecular docking. We thank Prof. Hao Wang and Prof. Zhiyuan Hu from NCNST for their kindly help for this work.

Appendix A. Supplementary data

Supplementary data to this article can be found online at https://doi.org/10.1016/j.bios.2021.113235.

References

Brabletz, T., Kalluri, R., Nieto, M.A., Weinberg, R.A., 2018. Nat. Rev. Cancer 18, 128–134.
Cheng, D.B., Zhang, X.H., Gao, Y.J., Ji, L., Hou, D.Y., Wang, Z.Q., Xu, W.H., Qiao, Z.Y., Wang, H., 2019. J. Am. Chem. Soc. 141, 7235–7239.
Dobson, C.M., 2003. Nature 426, 884–890.
Fan, X.Y., Liu, Y.J., Cai, Y.M., Wang, A.D., Xia, Y.Z., Hu, Y.J., Jiang, F.L., Liu, Y., 2019. Bioorg. Med. Chem. 27, 760–768.
Hartgerink, J.D., Beniash, E., Stupp, S.I., 2001. Science 294, 1684–1688.
Jajoo, R., Jung, Y., Huh, D., Viana, M.P., Rafelski, S.M., Springer, M., Paulsson, J., 2016. Science 351, 169–172.
James, D.T., Cameron, M., Kyle, J.L., 2019. J. Am. Chem. Soc. 141, 4886–4899.
Jeena, M.T., Jeong, K., Go, E.M., Cho, Y., Lee, S., Jin, S., Hwang, S.W., Jang, J.H., Kang, C.S., Bang, W.Y., Lee, E., Kwak, S.K., Kim, S., Ryu, J.H., 2019. ACS Nano 13, 11022–11033.
Jeena, M.T., Palanikumar, L., Go, E.M., Kim, I., Kang, M.G., Lee, S., Park, S., Choi, H., Kim, C., Jin, S.M., Bae, S.C., Rhee, H.W., Lee, E., Kwak, S.K., Ryu, J.H., 2017. Nat. Commun. 8, 10.
Li, C.-C., Liu, W.-X., Hu, J., Zhang, C.-Y., 2019a. Chem. Sci. 10, 8675–8684.
Li, X., Shi, L., Li, L., Dong, C., Li, C.-z., Shuang, S., 2019b. J. Anal. Testing 3, 37–49.
Lim, J.M., Heo, N.S., Oh, S.Y., Ryu, M.Y., Seo, J.H., Park, T.J., Huh, Y.S., Park, J.P., 2018. Biosens. Bioelectron. 99, 289–295.
Liu, M., Wang, Z.Y., Pan, L.Q., Cui, Y.P., Liu, Y.M., 2015. Biosens. Bioelectron. 69, 142–147.
Liu, Y., Lu, Y., Zhu, X., Li, C., Yan, M., Pan, J., Ma, G., 2020. Biomaterials 242, 119933.
Luo, S., Feng, J.X., Xiao, L.Y., Guo, L., Deng, L., Du, Z.W., Xue, Y., Song, X., Sun, X., Zhang, Z.R., Fu, Y., Gong, T., 2020. Biomaterials 249, 15.
Otake, S., Okuro, K., Bochicchio, D., Pavan, G.M., Aida, T., 2018. Bioconjugate Chem. 29, 2068–2073.
Park, E.J., Song, J.W., Kim, H.J., Kim, C.S., Song, Y.J., Yang, D.H., Yoo, H., Kim, J.W., Park, K., 2020. J. Ind. Eng. Chem. 92, 158–166.
Peri, S.S.S., Sabnani, M.K., Raza, M.U., Urquhart, E.L., Ghaffari, S., Lee, J.S., Kim, M.J., Weidanz, J., Alexandrakis, G., 2021. Nanotechnology 32, 045501.
Pigliacelli, C., Sanjeeva, K.B., Nonappa, Pizzi, A., Gori, A., Bombelli, F.B., Metrangolo, P., 2019. ACS Nano 13, 2158–2166.
Ren, T.T., Zhang, W., Liu, X.P., Zhao, H., Zhang, J., Zhang, J., Li, X., Zhang, Y., Bu, X., Shi, M., Yao, L.B., Su, J., 2014. J. Pathol. 234, 526–537.
Shah, B.P., Pasquale, N., De, G.J., Tan, T., Ma, J.J., Lee, K.B., 2014. ACS Nano 8, 9379–9387.
Shin, S., Gu, M.L., Yu, C.Y., Jeon, J., Lee, E., Choi, T.L., 2018. J. Am. Chem. Soc. 140, 475–482.
Shuaib, S., Saini, R.K., Goyal, D., Goyal, B., 2020. J. Biomol. Struct. Dyn. 38, 708–721.
Song, Y., Li, Y., Liu, Z.P., Liu, L.L., Wang, X.Y., Su, X.G., Ma, Q., 2014. Biosens. Bioelectron. 61, 9–13.
Song, Y., Shi, Q., Zhu, C., Luo, Y., Lu, Q., Li, H., Ye, R., Du, D., Lin, Y., 2017. Nanoscale 9, 15813–15824.
Tsai, J.H., Donaher, J.L., Murphy, D.A., Chau, S., Yang, J., 2012. Cancer Cell 22, 725–736.
Tu, M.M., Lee, F.Y.F., Jones, R.T., Kimball, A.K., Saravia, E., Graziano, R.F., Coleman, B., Menard, K., Yan, J., Michaud, E., Chang, H., Abdel-Hafiz, H.A., Rozhok, A.I., Duex, J. E., Agarwal, N., Chauca-Diaz, A., Johnson, L.K., Ng, T.L., Cambier, J.C., Clambey, E. T., Costello, J.C., Korman, A.J., Theodorescu, D., 2019. Sci. Adv. 5, eaav2437.
Walsh, L.A., Nawshad, A., Medici, D., 2011. Matrix Biol. 30, 243–247.
Wang, M., Wang, J., Zhou, P., Deng, J., Zhao, Y., Sun, Y., Yang, W., Wang, D., Li, Z., Hu, X., King, S.M., Rogers, S.E., Cox, H., Waigh, T.A., Yang, J., Lu, J.R., Xu, H., 2018. Nat. Commun. 9, 5118.
Wang, W.Z., Hu, Z.Y., 2019. Adv. Mater. 31, 8.
Wang, W.Z., Wei, Z.W., Zhang, D., Ma, H.L., Wang, Z.H., Bu, X.L., Li, M.L., Geng, L.L., Lausted, C., Hood, L., Fang, Q.J., Wang, H., Hu, Z.Y., 2014. Anal. Chem. 86, 11854–11859.
Wei, X., Liu, L., Guo, X., Wang, Y., Zhao, J., Zhou, S., 2018. ACS Appl. Mater. Interfaces 10, 17672–17684.
Yang, Y., Yue, C., Han, Y., Zhang, W., He, A., Zhang, C., Yin, T., Zhang, Q., Zhang, J., Yang, Y., Ni, J., Sun, J., Cui, D., 2016. Adv. Funct. Mater. 26, 8735–8745.
Ying, Z.M., Yuan, Y.Y., Tu, B., Tang, L.J., Yu, R.Q., Jiang, J.H., 2019. Chem. Sci. 10, 4828–4833.
Yue, C., Zhang, C., Alfranca, G., Yang, Y., Jiang, X., Yang, Y., Pan, F., de la Fuente, J.M., Cui, D., 2016. Theranostics 6, 456–469.
Zhang, K., Corsa, C.A., Ponik, S.M., Prior, J.L., Piwnica-Worms, D., Eliceiri, K.W., Keely, P.J., Longmore, G.D., 2013. Nat. Cell Biol. 15, 677–687.
Zhang, L., Jing, D., Jiang, N., Rojalin, T., Baehr, C.M., Zhang, D., Xiao, W., Wu, Y., Cong, Z., Li, J.J., Li, Y., Wang, L., Lam, K.S., 2020. Nat. Nanotechnol. 15, 145–153.
Zhang, P., Wang, J., Chen, H., Zhao, L., Chen, B., Chu, C., Liu, H., Qin, Z., Liu, J., Tan, Y., Chen, X., Liu, G., 2018a. J. Am. Chem. Soc. 140, 14980–14989.
Zhang, S.G., 2003. Nat. Biotechnol. 21, 1171–1178.
Zhang, X., Wang, H., Antaris, A.L., Li, L., Diao, S., Ma, R., Nguyen, A., Hong, G., Ma, Z., Wang, J., 2016. Adv. Mater. 28, 6872–6879.
Zhang, X.J., Miao, Z.Y., Hu, Y., Yang, X.T., Tang, Y.Y., Zhu, D., 2018b. Sens. Actuators B Chem. 273, 511–518.
Zhao, Y., Hu, X., Zhang, L., Wang, D., King, S.M., Rogers, S.E., Wang, J., Lu, J.R., Xu, H., 2020. J. Colloid Interface Sci. 583, 553–562.